



Published in final edited form as:

*J Am Chem Soc.* 2011 April 6; 133(13): 5062–5075. doi:10.1021/ja110842s.

## Transition State Charge Stabilization Through Multiple Non-Covalent Interactions in the Guanidinium-Catalyzed Enantioselective Claisen Rearrangement

Christopher Uyeda and Eric N. Jacobsen\*

Harvard University, Department of Chemistry & Chemical Biology, Cambridge, MA 02138.

### Abstract

The mechanism by which chiral arylpyrrole-substituted guanidinium ions promote the Claisen rearrangement of *O*-allyl  $\alpha$ -ketoesters and induce enantioselectivity was investigated by experimental and computational methods. In addition to stabilization of the developing negative charge on the oxallyl fragment of the rearrangement transition state by hydrogen-bond donation, evidence was obtained for a secondary attractive interaction between the  $\pi$ -system of a catalyst aromatic substituent and the cationic allyl fragment. Across a series of substituted arylpyrrole derivatives, enantioselectivity was observed to vary predictably according to this proposal. This mechanistic analysis led to the development of a new *p*-dimethylaminophenyl-substituted catalyst, which afforded improvements in enantioselectivity relative to the parent phenyl catalyst for a representative set of substrates.

### Introduction

Since its initial report nearly a century ago, the [3,3]-sigmatropic rearrangement of allyl vinyl ethers—the Claisen rearrangement—has been applied extensively in the synthesis of structurally and stereochemically complex organic molecules.<sup>1</sup> A principle feature of the Claisen rearrangement that underlies its synthetic utility is the high and predictable diastereoselectivity imparted by the pericyclic mechanism, allowing  $\alpha$ - and  $\beta$ -stereogenic carbonyl compounds of either the *syn* or *anti* relative configuration to be prepared from precursors bearing the appropriate alkene geometries. While early efforts to obtain enantioenriched Claisen rearrangement products were focused on the use of chiral substrates, particularly those derived from secondary allylic alcohols, asymmetric methods involving metal-based catalysts have recently been developed.<sup>2,3,4</sup> Limitations in the scope of these reactions persist, however, due to challenges associated with competing background rearrangement and the strong binding affinity of the products to the catalysts. Allyl vinyl ether substrates are also susceptible to fragmentation in the presence of catalysts that are either strongly Lewis acidic or promote the formation of  $\pi$ -allyl metal species, and the dissociated intermediates are often observed to recombine to form mixtures of regioisomeric [1,3]- and diastereomeric [3,3]-rearrangement products.

jacobsen@chemistry.harvard.edu.

**Supporting Information Available:** Complete experimental procedures; characterization data including <sup>1</sup>H- and <sup>13</sup>C-NMR spectra for catalysts, substrates, and products; chromatographic traces for enantioselective rearrangements; data for kinetic and binding studies; geometries and energies of all calculated stationary points; and complete ref 25. This material is available free of charge via the Internet at <http://pubs.acs.org>.

Chorismate mutases accelerate the Claisen rearrangement of chorismate to prephenate on the order of a million-fold by a mechanism that involves the formation of multiple non-covalent interactions between the enzyme and substrate. X-ray structures of *Bacillus subtilis*<sup>5a,b</sup> (BsCM) and *Escherichia coli*<sup>5c</sup> chorismate mutases co-crystallized with the oxa-bicyclic transition state analog **1**<sup>6</sup> have led to the identification of arginine and/or lysine residues in the active site that are positioned to interact with the core heteroatom of the allyl vinyl ether system as well as the pendant carboxylate functional groups (Scheme 1). While the relative contributions of selective transition state stabilization and substrate conformational effects in the mechanism of catalysis have not been definitively elucidated,<sup>7</sup> mutagenesis studies have established the critical importance of these cationic hydrogen-bond donor residues. Several BsCM mutants that incorporate lysine at position 90 or the nearby position 88 are also catalytically competent;<sup>8a</sup> however, the Arg90Ala single-point mutant exhibits no chorismate mutase activity.<sup>8b</sup> Furthermore, the replacement of Arg 90 with citrulline, an isosteric urea-containing residue that is charge-neutral, results in an over ten thousand-fold decrease in rate, while ground state binding to **1** is minimally disrupted.<sup>9</sup>

Electrostatic stabilization of the developing positive charge on the allyl fragment of the rearrangement transition state has also been proposed as a complementary mechanism of catalysis by chorismate mutases. The active site of BsCM in particular contains a phenylalanine residue, which is potentially oriented to provide  $\pi$ -stabilization, at a 3.59 Å C–C distance from the transition state analog.<sup>5b</sup>

Despite the fact that valuable mechanistic insight has been gleaned from structural studies of chorismate mutases bound to inhibitors that are geometric mimics of the rearrangement transition state, these analogs possess neither the charge distribution nor the dissociated structure of the actual pericyclic transition state. Catalytic antibodies developed using such inhibitors display modest activity compared to the wild-type enzyme,<sup>10</sup> an observation that has been attributed to poor electrostatic stabilization of the dipolar transition state.<sup>11</sup> The active site of the 1F7 antibody, for example, contains only a single cationic hydrogen-bond donor that is likely occupied in a salt bridge with a carboxylate group.<sup>12</sup>

As a complement to these studies of Claisen rearrangements mediated by biological macromolecules, we have investigated non-covalent catalyst–transition state interactions in the context of small molecule hydrogen-bond donors that have the advantages of being readily accessible by synthesis and amenable to modeling using high-level computational methods. Guided in part by the proposed mechanism of substrate activation by chorismate mutases, simple guanidinium ion derivatives were identified as effective catalysts for the [3,3]-sigmatropic rearrangement of a variety of substrates in non-polar organic solvents.<sup>13</sup> Allyl vinyl ethers bearing substituents that promote dipolar transition structures were found to be particularly amenable to catalysis by such hydrogen-bond donors.<sup>14,15</sup> We subsequently identified and optimized chiral, C<sub>2</sub>-symmetric guanidinium ion derivatives as catalysts for enantioselective rearrangements of chorismate analogs with carboxyl substitution on the vinyl group (Scheme 2). Pyrrolo-*trans*-diaminocyclohexane-derived guanidinium ions bearing aryl substituents at the 2-position of the pyrrole group (e.g., **2**) were found to be particularly effective, displaying significantly higher reactivity and enantioselectivity relative to pyrrole derivatives such as **3** that bear aliphatic substituents. This empirical observation pointed to the intriguing possibility of a secondary stabilizing role of catalyst aromatic substituents in the Claisen rearrangement transition state. Such an interaction would be analogous to that proposed for an active site phenylalanine residue in BsCM<sup>5b</sup> and is also preceded in the association of both ground state and transition state cations to aromatic  $\pi$ -systems in other well-characterized protein complexes.<sup>16</sup>

In an effort to elucidate the non-covalent interactions that are responsible for rate acceleration and asymmetric induction in guanidinium-catalyzed rearrangements of *O*-allyl  $\alpha$ -ketoesters, we have carried out kinetic analyses and quantitative catalyst structure–enantioselectivity relationship studies in combination with computational transition state modeling. A mechanistic picture emerges in which hydrogen-bonding interactions with the Lewis-basic heteroatoms of the substrate operate cooperatively with  $\pi$ -stabilization of the cationic charge developing on the allyl fragment in the energetically favored rearrangement transition state.

## Results and Discussion

### Kinetic Studies of Guanidinium-Catalyzed Rearrangements

The model *O*-crotyl 2-oxobutyrates substrate **5** was observed to undergo a [3,3]-sigmatropic rearrangement catalyzed by 20 mol% (***R,R***)-**2** to afford **6** in 73% enantiomeric excess (ee) and a > 20:1 diastereomeric ratio (d.r.). The methyl-substituted catalyst (***R,R***)-**3** exhibited both measurably decreased activity and enantioselectivity (Table 1, entry 2).<sup>17</sup> The product stereochemistry was established as (*S,S*) by X-ray analysis of a crystalline iodoether derivative, the relative configuration being consistent with rearrangement through a chair-like six-membered transition structure. In hexanes, the catalyst is completely insoluble even in the presence of the substrate, suggesting that reactions in this medium occur in the precipitated catalyst phase. Despite the aggregated state of the catalyst, no evidence for diastereomeric interactions between multiple guanidinium ions was found either in the ground state or the rearrangement transition state, as reactions conducted with scalemic mixtures of catalyst **2** displayed a strictly linear dependence of product ee on catalyst ee and nearly identical rates.<sup>18,19</sup>

In other non-polar organic solvents (Table 1, entries 3–5), where the catalyst is either partially or completely soluble, rearrangements proceeded with slightly diminished enantioselectivity. The uncatalyzed rate was found to be significantly higher in these solvents, however, suggesting that the lower product ee is primarily a consequence of competing background rearrangement. In accord with this hypothesis, enantioselectivities for reactions conducted in hexanes and CDCl<sub>3</sub> were observed to converge as the catalyst loading was increased (Figure 1). In more Lewis basic solvents such as *tert*-butyl methyl ether (TBME), which is capable of binding to the guanidinium ion in competition with the substrate, low levels of catalysis were observed. The similarity in enantioselectivity across a range of non-polar, non-coordinating solvents and under both heterogeneous and homogeneous conditions suggests a common mechanism of catalysis and asymmetric induction that is unlikely to involve the explicit participation of solvent molecules in the rearrangement transition state.

In order to establish the stoichiometry of the catalyzed rearrangement transition state and identify catalyst resting states for the reaction of **5** catalyzed by (***R,R***)-**2**, kinetic studies were performed under fully homogenous conditions in CDCl<sub>3</sub>.<sup>20,21</sup> We conducted a series of experiments using a constant initial substrate **5** concentration of 0.05 M and variable loadings of (***R,R***)-**2** from 0–30 mol%, monitoring the concentrations of both the substrate and the product by <sup>1</sup>H-NMR (Figure 2).<sup>22</sup> All rearrangements proceeded without the formation of detectable side products, and no decomposition of the catalyst was detectable spectroscopically over the course of the reaction.

The uncatalyzed rearrangement exhibits simple first order rate dependence on [**5**], with a rate constant ( $k_{\text{uncat}}$ ) of  $1.42 \times 10^{-5} \text{ s}^{-1}$ . By application of the Eyring equation, an activation free energy ( $\Delta G_{328}^{\ddagger}$ ) of 26.5 kcal/mol was calculated.<sup>23</sup> Using initial reaction rates measured over the first 10% conversion,  $k_{\text{uncat}}$  in hexanes was determined to be  $2.11 \times 10^{-6}$

$s^{-1}$  at the same temperature, corresponding to a  $\Delta G_{328}^{\ddagger}$  of 27.8 kcal/mol. Similar sensitivity of rate to solvent polarity has been observed for other pericyclic reactions that proceed through transition states that are substantially more polarized than the ground state.<sup>14,24</sup>

The rate data for rearrangements catalyzed by **(R,R)-2** are consistent with first-order dependence on the total catalyst concentration and saturation behavior in the substrate.

Rearrangements were also conducted at a constant **(R,R)-2** total concentration of 0.01 M and initial concentrations of substrate **5** ranging from 0.05–0.2 M (Figure 3). The lack of overlay between the rate curves suggests substantial inhibition by product **6**, which accumulates over the course of the reaction.<sup>20</sup> The contributions of various catalyst resting states to reaction rate were quantified by fitting the data from all ten kinetics experiments to a rate law of the general form shown in eq 1 ( $R^2 = 0.989$ ), which contains terms for an uncatalyzed unimolecular rearrangement and a catalyst-mediated rearrangement.

$$\text{rate} = -\frac{d[\mathbf{5}]}{dt} = \frac{a[(\mathbf{R,R})\text{-}\mathbf{2}]_{\text{tot}}[\mathbf{5}]}{1+b[\mathbf{5}]+c[\mathbf{6}]} + k_{\text{uncat}}[\mathbf{5}] \quad (1)$$

Exchange between unbound and various bound states of the catalyst was found to be fast on the <sup>1</sup>H-NMR time scale at 55 °C, indicating that the rates of catalyst association and dissociation processes are faster by several orders of magnitude than the rate of rearrangement. It is, therefore, possible to apply an equilibrium approximation to the data in order to estimate binding constants for the kinetically relevant catalyst complexes (Scheme 3). From the kinetic parameters, the association constant ( $K_a$ ) of the substrate–catalyst complex **(R,R)-2•5** was calculated to be 1.7 times greater than the value for the product–catalyst complex **(R,R)-2•6**. The  $k_{\text{cat}}/k_{\text{uncat}}$  deduced from these data is 37, which corresponds to a 2.3 kcal/mol lowering of the activation free energy at 328 K. In hexanes, a  $k_{\text{cat}}/k_{\text{uncat}}$  of 250 was approximated, under the assumption that the rate constant for the catalyzed rearrangement is independent of solvent; at high catalyst loadings, reactions in CDCl<sub>3</sub> and hexanes proceed to similar levels of conversion at 40 °C after 14 h (Figure 1).

The rate profile for catalyst **(R,R)-2** was compared to that of the methyl-substituted catalyst **(R,R)-3** as well as the *N,N'*-dicyclohexylguanidinium catalyst **4** (Figure 4). Both of these guanidinium ions exhibit significantly lower catalytic activity than **(R,R)-2**, suggesting that while the presence of the pyrrole functional group does not affect the rate, the phenyl substituent plays a significant role in lowering the activation barrier for the rearrangement.

### Computational Studies with a Simplified Model Guanidinium Catalyst

The effect of guanidinium ion catalysis on the structures and relative energies of Claisen rearrangement transition states was further investigated by computational methods using Gaussian 03.<sup>25</sup> We first examined the mechanism of the uncatalyzed rearrangement of **5** at the B3LYP/6-31G(d) level of density functional theory (DFT), which has been utilized extensively to model pericyclic reactions and has been validated against experimental kinetic isotope effect and activation energy data.<sup>26,27</sup> Stationary points were located for the substrate, chair-like rearrangement transition state, and product with both an *s-trans* and *s-cis* stereochemical relationship between the vinyl ether and ester groups (Figure 5).<sup>28,29</sup> For the substrate and transition state, very small energetic differences of < 1 kcal/mol were calculated between the two conformations; however, a more significant difference in energy of 1.8 kcal/mol between the *s-trans* and *s-cis* conformations of the product was determined.<sup>30</sup>

An activation energy ( $\Delta E^\ddagger$ ) of 27.4 kcal/mol was calculated for the uncatalyzed rearrangement; from frequency calculations,  $\Delta G^\ddagger_{298}$  was estimated to be 28.2 kcal/mol. Boat-like transition structures were also optimized and are approximately 4 kcal/mol higher in energy, consistent with the high levels of diastereoselectivity observed in these rearrangements.

In order to establish plausible modes of interaction between the guanidinium functional group and the substrate, a simplified catalyst, *N,N'*-dimethylguanidinium ion (**7**), was modeled. Catalyst complexes of the *s-cis* conformational series are consistently lower in energy than for the *s-trans* series by > 4 kcal/mol, indicating that hydrogen-bonding to the ester carbonyl is energetically favored. The calculated activation energy for the rearrangement is lowered by 4.4 kcal/mol in the guanidinium-catalyzed pathway relative to the uncatalyzed pathway. In the catalyst-bound transition state complex, the length of the hydrogen-bond between the catalyst and the ether oxygen is decreased by 0.08 Å relative to the ground state.<sup>31</sup> This shortening of the hydrogen-bonding distance can be rationalized by greater electrostatic stabilization of the developing negative charge in the transition state. By contrast, a negligible geometric change (0.01 Å) is observed in the interaction with the ester carbonyl.

Optimized geometries for thermal and *N,N'*-dimethylguanidinium-catalyzed rearrangement transition structures are shown in Figure 6. Compared to the transition structure for unsubstituted allyl vinyl ether, *s-cis*-TS-**5** is substantially more dissociated, with longer breaking C–O and forming C–C bond distances. Estimates of the partial charges on the allyl and oxallyl fragments using the Mulliken, Natural Bond Orbital (NBO),<sup>32</sup> and CHELPG<sup>33</sup> methods of population analysis consistently indicate increased dipolar character as a consequence of ester substitution. In the presence of the guanidinium ion, the partial C–O and C–C bond distances are further lengthened by approximately 0.1 Å, and a fraction of the guanidinium ion positive charge is delocalized primarily into the allyl fragment of the rearrangement transition state.

As a point of comparison, the lowest-energy transition structure for the *N,N'*-3,5-bis(trifluoromethyl)phenylthiourea- (**8**) catalyzed rearrangement is also shown in Figure 6. In accord with earlier observations that *N*-aryl urea and thiourea derivatives such as **8** display little catalytic activity in the rearrangement of *O*-allyl  $\alpha$ -ketoesters,<sup>13,15b</sup> the calculated activation energy as well as distance and charge metrics for **8**•*s-cis*-TS-**5** are intermediate between those for the uncatalyzed (*s-cis*-TS-**5**) and *N,N'*-dimethylguanidinium catalyzed (**7**•*s-cis*-TS-**5**) transition states.

## Structure and Conformations of Catalyst 2

Having established a basic model for the hydrogen-bonding interactions between a simplified guanidinium ion, **7**, and the substrate, we turned our attention to studies involving the chiral catalyst **2**. The geometry of the cation was optimized computationally at the B3LYP/6-31G(d) level of theory, and minima were located for various rotamers about the guanidinium ion C–N bonds as well as the pyrrole–cyclohexane C–N bond. In the lowest-energy structure, shown in Figure 8, the guanidinium functional group is disposed in a (*Z,Z*)-conformation, consistent with both an X-ray structure that was previously obtained<sup>13</sup> for (*R,R*)-**2** (Figure 7(A)) and ROESY cross-peaks that were observed for a catalyst solution in CDCl<sub>3</sub> (Figure 7(B)).

The guanidinium ion NH<sub>2</sub> hydrogens reside in close contact with the  $\pi$ -faces of the pyrrole rings: there is a 3.23 Å distance between the guanidinium nitrogen and nearest carbon atom of the pyrrole in the calculated structure—these distances are 3.22 and 3.19 Å in the crystal structure.<sup>34</sup> This intramolecular interaction influences the degree to which the cyclohexane



ring is canted with respect to the plane of the guanidinium ion and places the phenyl groups in proximity to the substrate binding site. The sensitivity of the energy of this structure to deviations from the ground state geometry was probed by computationally scanning the dihedral angle defined by the C–NH<sub>2</sub> bond of the guanidinium group and the axial C–H bond of the cyclohexane ring, highlighted in red in Figure 8. We performed constrained optimizations at 5° dihedral increments, and the relative energies were calculated for both (*R,R*)-**2** and *N,N'*-dicyclohexylguanidinium ion **4**. It is evident from the comparison of these two scans that for (*R,R*)-**2**, rotation of the dihedral angle in the negative direction is hindered by repulsive interactions between the guanidinium ion and the pyrrole, and rotation in the positive direction is disfavored due to weakening of the guanidinium–pyrrole interaction.

### Ground State Binding Interactions

Kinetic data presented above were consistent with an initial, reversible binding of the substrate to the catalyst prior to the rate-limiting sigmatropic rearrangement. At 22 °C, the rearrangement of **5** in the presence of (*R,R*)-**2** was sufficiently slow to allow the substrate–catalyst complex to be studied directly by <sup>1</sup>H-NMR. A selected region of the spectra for a series of equimolar solutions of **5** and (*R,R*)-**2** in a concentration range of 0.1–0.00026 M is shown in Figure 9(A). At the high-concentration limit of the experiment, the signal corresponding to the guanidinium *N*-H<sup>a</sup> protons is shifted downfield by approximately 1.5 ppm relative to the free catalyst, consistent with a binding event that involves a hydrogen-bonding interaction to the substrate.<sup>35</sup> A similar shift was observed for dilution experiments performed with 80% ee (*S,S*)-**6** (Figure 9(C)). By comparison, the chemical shift of the *N*-H<sup>b</sup> protons of the guanidinium –NH<sub>2</sub> group at 3.5 ppm, remains relatively unchanged. The methylene protons (H<sup>d</sup>) of **5**, which appear as a doublet for the free substrate, become diastereotopic and undergo a > 1 ppm upfield shift upon complexation, suggesting an intimate association with the chiral framework of the catalyst.

More detailed structural insight into the (*R,R*)-**2**•**5** complex was obtained by computational optimization of its geometry. In the lowest-energy structure, the substrate is in a pro-(*S,S*) conformation, and the methylene group is located in proximity to the π-faces of the catalyst phenyl substituents (Figure 10). The closest contact between a substrate hydrogen atom and a carbon atom of the phenyl ring is 3.0 Å. This geometry provides a rationale for the spectroscopically observed complexation-induced upfield shift of the substrate signals corresponding to the methylene group protons, H<sup>d</sup>.<sup>36</sup>

The chemical shift data for the methyl ester singlet (H<sup>c</sup>) of **5** over the entire concentration range of the dilution experiment provided a good fit to a 1:1 binding model ( $R^2 = 0.996$ ), and a  $K_a$  of 218 M<sup>-1</sup> was calculated.<sup>37</sup> A 1:1 stoichiometry for the complex was further established by the method of continuous variation (Job's plot).<sup>38,39</sup> The same dilution procedure was repeated for the complexes between 80% ee (*S,S*)-**6** and each enantiomer of catalyst **2** (Table 2). The two diastereomeric catalyst–product complexes were thus found to exhibit nearly identical binding constants. The  $K_a$  for **5** was determined to be roughly twice the value as compared to **6**, corresponding to a 0.41 kcal/mol energetic preference for substrate binding over product binding. The relative values of these binding free energies measured at 22 °C are consistent with those extracted from the kinetic data at 55 °C.

### Computational Model for the Enantioselective Rearrangement

Having established the basic stoichiometry of the catalyzed rearrangement transition state from kinetics experiments and examined ground state binding interactions, we next conducted computational modeling studies with the full structure of catalyst **2** in order to gain more detailed insight into the origin of asymmetric induction. Of particular interest was a rationale for the beneficial effect of the catalyst phenyl substituent on both rate and

enantioselectivity. Geometries of the catalyst-bound substrate, rearrangement transition state, and product were fully optimized in the gas phase at the B3LYP/6-31G(d) level of DFT. Relative energies for these structures, leading to both the experimentally observed major (*S,S*) and minor (*R,R*) enantiomers of product **6**, are shown in Figure 11.

The energy difference between the two diastereomeric rearrangement transition state complexes ( $\Delta\Delta E^\ddagger$ ) was calculated to be 2.99 kcal/mol, with the pro-(*S,S*) transition state being the lowest in energy. Detailed representations of these structures are shown in Figure 12. In both complexes, the oxallyl fragment is roughly planar with respect to the guanidinium ion of the catalyst, and the allyl fragment is either projected toward the phenyl substituent of the pyrrole in the case of the major transition state (A), or toward the cyclohexanediamine backbone in the minor transition state (B). The energetic preference for interaction of the allyl fragment with the phenyl group vs. the cyclohexane ring provides a plausible explanation for the calculated difference in transition state energies. In the major transition structure, the closest distance between a C-H of the allyl fragment and the centroid of the phenyl ring is 2.98 Å, placing it within an appropriate distance for an attractive interaction.<sup>40</sup>

Single-point energies for the two transition states were also calculated using a larger basis set as well as the MP2 method in order to establish that the model for selectivity is robust across different levels of theory. The transition structures were also fully optimized using the M05-2X functional. These results are summarized in Table 3. All computational methods are in agreement with respect to the sense of enantioinduction and accurately predict the observed absolute configuration of the product. The magnitudes of  $\Delta\Delta E^\ddagger$ , while narrowly distributed, consistently overestimate the experimental enantioselectivity. These discrepancies might be due to neglect of entropic contributions and medium effects in the computational model. Regardless of the source of the calculated overestimation of ee, it is expected that many of the errors associated with these approximations cancel out in the analysis of selectivity trends across different catalyst structures.

The geometries of the pro-(*S,S*) and pro-(*R,R*) transition structures were also optimized for the methyl-substituted pyrrole catalyst (**R,R**)-**3**, and the  $\Delta\Delta E^\ddagger$  was calculated to be 2.29 kcal/mol at the B3LYP/6-31G(d) level of theory.<sup>41</sup> From the comparison of this value to that obtained for (**R,R**)-**2**, the interaction of the phenyl substituent with the allyl fragment can be estimated to provide approximately 0.7 kcal/mol of stabilization to the major transition state. As an alternative explanation, the lower enantioselectivity both observed and calculated for catalyst (**R,R**)-**3** might be rationalized on the basis of repulsive non-bonding interactions with the methyl group in the major transition state. However, the distance between the closest hydrogen atoms on the methyl group and the allyl fragment in the geometry-optimized structure is 2.56 Å, placing them outside of van der Waals contact.<sup>42</sup> Furthermore, such a steric transition state destabilization model would predict decreased reactivity for the 2-methylpyrrole-bearing catalyst (**R,R**)-**3**; in fact kinetic studies revealed that (**R,R**)-**3** catalyzed the rearrangement with a similar rate to the *N,N'*-dicyclohexylguanidinium catalyst **4**.

### Electronically-Substituted Arylpyrrole Catalysts

In order to devise an experimental test of the proposed stabilizing role of the catalyst phenyl substituent in the lowest-energy diastereomeric transition state, we prepared and evaluated a series of arylpyrrole catalysts bearing substitution that was expected to perturb this interaction (**9a-d**, **10a-b**, Table 4)). Substituent effects on the strength and geometry of ground state cation- $\pi$  interactions have been modeled computationally and studied experimentally by the measurement of gas phase interactions energies and solution phase

binding constants; however, few reports have described the systematic characterization of these effects for transition states with cationic character.<sup>43,44,45</sup>

Enantioselectivities were determined for reactions performed in hexanes at 40 °C using 20 mol% catalyst loading (Table 4). For all catalysts, rearrangements under these conditions proceeded to high levels of conversion relative to the thermal rearrangement conducted in the absence of catalyst, indicating that the trends that were observed are related to the intrinsic enantioselectivity of the catalyzed pathway rather than variable amounts of competing racemic background reaction. Catalyst **9b**, which contains an electron-donating 4-dimethylamino substituent provided higher levels of enantioselectivity than **2**, while catalyst **9a**, with an inductively withdrawing 4-fluoro substituent, exhibited the opposite effect. Polyfluorinated catalysts **9c** and **9d** afforded particularly low enantioselectivities compared to the parent catalyst. Direct substitution of the pyrrole ring was also explored with either a donating methyl or withdrawing trifluoromethyl group (**10a** and **10b**).

Enantioselectivities were also determined computationally at the B3LYP/6-31G(d) level of theory from the energy difference between diastereomeric transition states of the general structure shown in Figure 12.<sup>46</sup> Although the overall trend in enantioselectivity was reproduced, poor quantitative correspondence was observed between calculated and experimental results (Figure 13).<sup>47</sup> Because of the well-established limitations of the B3LYP functional in accurately reproducing the energy of weak non-covalent interactions such as cation- $\pi$  interactions, transition structures for all catalysts were also fully optimized using the M05-2X functional, which has been specifically parameterized for such purposes.<sup>48</sup> Using the latter method, significantly higher correlation ( $R^2 = 0.88$ ) with experimental data was observed (Figure 14).

Electrostatic potential maps were generated for a representative sample of arylpyrrole structures in order to provide a qualitative model for the observed trend in enantioselectivity (Figure 15). Dougherty has shown that variations in ground state binding energies between alkali metal cations and substituted arenes can be largely correlated with the electrostatic component of the interaction.<sup>43</sup> The most selective catalyst, **9b**, has significantly greater negative potential above the  $\pi$ -face of the arene, while the fluorinated catalysts have significantly less negative potential. For the pentafluorophenyl catalyst **9d**, the electrostatic component of the interaction between the cationic allyl fragment and the  $\pi$ -system is expected to be repulsive.

A comparison of the optimized geometries of the major pro-(*S,S*) transition structures for the phenyl catalyst **2** and pentafluorophenyl catalyst **9d** at the M05-2X level of DFT are shown in Figure 16. For **9d**, the distance between the closest hydrogen atom of the allyl fragment to the centroid of the arene is significantly lengthened to 3.26 Å, compared to 2.59 Å for the phenyl-substituted catalyst **2**. A second pro-(*S,S*) transition structure of lower energy, by 0.6 kcal/mol, was located in which the oxallyl group of the substrate is nearly perpendicular relative to the plane of the guanidinium ion (Figure 16(B)). Although the hydrogen-bond angles are far from ideal in this transition structure, the electrostatic interaction between the allyl group and the fluoroarene is more favorable with a 2.27 Å distance between a hydrogen atom on the allyl group and a meta-fluorine substituent. Similar geometries for interactions between highly fluorinated arenes and both early transition-metal cations<sup>49</sup> as well as arene C-H bonds<sup>50</sup> have been observed crystallographically.

### Substrate Scope with the Dimethylamino-Substituted Catalyst **9b**

Having established the importance of catalyst electronic effects on the enantioselective rearrangement of model substrate **5**, we compared (*R,R*)-**2** and the dimethylamino-substituted catalyst (*R,R*)-**9b** for a representative set of rearrangements. Small increases in



enantioselectivity, corresponding to an average free energy of  $0.19 \pm 0.08$  kcal/mol for entries in Table 6, were consistently observed across a range of *O*-allyl  $\alpha$ -ketoesters with different olefin substitution patterns. Substrates were selected that form products with  $\alpha$ -stereogenic centers of different steric demands (entries 1 and 2), vicinal tertiary stereogenic centers of both the *syn* and *anti* relative stereochemistry (entries 3–5), and  $\beta$ -quaternary stereogenic centers (entries 6 and 7).

## Conclusions

The phenylpyrrole-substituted guanidinium catalyst **2** induces a 3.6 kcal/mol lowering of the activation free energy for the rearrangement of **5**, as compared to the thermal rearrangement in hexanes, corresponding to a rate acceleration of approximately 250-fold. In computational models, guanidinium catalysts are seen to interact with the allyl vinyl ether substrate through hydrogen bonds with both the ether oxygen atom as well as the pendant ester group. This interaction allows stabilization of the developing negative charge in the transition state. For rearrangements catalyzed by **2**, a secondary interaction is evident in the major diastereomeric transition state between the  $\pi$ -system of the catalyst phenyl substituent and the cationic allyl fragment of the substrate. This proposal is supported by the experimental observation that **2** is both more enantioselective and more active than **3**, which lacks an appropriately positioned Lewis basic functional group. Furthermore, the strength of this interaction is rationally tunable through substitution of the arene. Thus, catalyst **9b**, which possesses a dimethylamino substituent, is more selective than **2** for a range of substrates with different olefin substitutions.

While the mechanistic model proposed here for rearrangements promoted by a synthetic small molecule catalyst bears striking analogy to the enzymatic rearrangement of chorismate, important differences are worth noting. The active sites of chorismate mutases are sufficiently recessed within the protein structure to allow these enzymes to extract substrates from an aqueous environment and engage them in a large number of non-covalent interactions in order to achieve high levels of catalytic activity as well as exquisite substrate specificity: chorismate mutases accelerate the rearrangement of chorismate over a million-fold; however, modifications to the pendant carboxylate or alcohol functionality of the substrate generally result in either a significant or complete loss of activity.<sup>51</sup> By contrast, the primary catalytic functional group, the guanidinium ion, of **2** is largely solvent-exposed, and in computationally-optimized transition structures, only the ester-substituted vinyl ether system and the methylene group of the substrate are intimately associated with the catalyst framework. As a consequence, these small-molecule catalysts only operate efficiently in non-polar media where desolvation energy is minimal and the strength of electrostatic interactions is maximized. While limited contacts with the substrate impose a constraint on rate acceleration, it allows the catalyst to accept a broader range of substrate structures.

In this study, experimentally-validated computational models for key enantioselectivity-determining steps have provided detailed insight into the operative molecular recognition processes in the guanidinium ion-catalyzed asymmetric Claisen rearrangement.<sup>52</sup> Enantioselectivity was found to rely on multiple, attractive interactions to differentially stabilize a single transition structure. Such cooperativity effects are emerging as a general principle in small-molecule hydrogen-bond donor catalysis.<sup>53</sup>

## Supplementary Material

Refer to Web version on PubMed Central for supplementary material.

## Acknowledgments

This work was supported by the NIH (GM 43214). We thank Matthew Rienzo for experimental assistance, and Dr. Shao-Liang Zheng for X-ray analysis.

## Notes and References

1. For reviews: Ziegler FE. *Chem. Rev.* 1988; 88:1423–1452. (b) Castro AMM. *Chem. Rev.* 2004; 104:2939–3002. [PubMed: 15186185] (c) Hiersemann, M.; Nubbemeyer, U., editors. *The Claisen Rearrangement*. Vol. 2007. Weinheim, Germany: Wiley-VCH;
2. Lewis acid-catalyzed enantioselective rearrangements of ester-substituted allyl vinyl ethers: Abraham L, Czerwonka R, Hiersemann M. *Angew. Chem. Int. Ed.* 2001; 40:4700–4703. (b) Abraham L, Körner M, Hiersemann M. *Tetrahedron Lett.* 2004; 45:3647–3650. (c) Linton EC, Kozlowski MC. *J. Am. Chem. Soc.* 2008; 130:16162–16163. [PubMed: 18998679] (d) Marié J-C, Xiong Y, Min GK, Yeager AR, Taniguchi T, Berova N, Schaus SE, Porco JA Jr. *J. Org. Chem.* 2010; 75:4584–4590. [PubMed: 20527786]
3. Catalytic enantioselective Claisen and related rearrangements proposed to proceed by olefin activation mechanisms: Akiyama K, Mikami K. *Tetrahedron Lett.* 2004; 45:7217–7220. (b) Geherty ME, Dura RD, Nelson SG. *J. Am. Chem. Soc.* 2010; 132:11875–11877. [PubMed: 20687554] (c) Calter M, Hollis TK, Overman LE, Ziller J, Zipp GG. *J. Org. Chem.* 1997; 62:1449–1456. (d) Anderson CE, Overman LE. *J. Am. Chem. Soc.* 2003; 125:12412–12413. [PubMed: 14531676]
4. Examples of enantioselective Claisen rearrangements with chiral reagents: Maruoka K, Banno H, Yamamoto H. *J. Am. Chem. Soc.* 1990; 112:7791–7793. (b) Maruoka K, Saito S, Yamamoto H. *J. Am. Chem. Soc.* 1995; 117:1165–1166. (c) Corey EJ, Lee DH. *J. Am. Chem. Soc.* 1991; 113:4026–4028. (d) Ito H, Sato A, Taguchi T. *Tetrahedron Lett.* 1997; 38:4815–4818. (e) Ito H, Sato A, Kobayashi T, Taguchi T. *Chem. Commun.* 1998:2441–2442. (f) Yoon TP, MacMillan DWC. *J. Am. Chem. Soc.* 2001; 123:2911–2912. [PubMed: 11456990]
5. (a) Chook Y-M, Ke H, Lipscomb WH. *Proc. Natl. Acad. Sci. U.S.A.* 1993; 90:8600–8603. [PubMed: 8378335] (b) Chook Y-M, Gray JV, Lipscomb WN. *J. Mol. Biol.* 1994; 240:476–500. [PubMed: 8046752] (c) Lee AY, Karplus A, Ganem B, Clardy J. 1995; 117:3627–3628.
6. Bartlett PA, Johnson CR. *J. Am. Chem. Soc.* 1985; 107:7792–7793.
7. Recent theoretical studies of the relative contribution of transition state stabilization in the enzymatic rearrangement of chorismate, and references therein: Ranaghan KE, Ridder L, Szeftczyk B, Sokalski WA, Hermann JC, Mulholland AJ. *Org. Biomol. Chem.* 2004; 2:968–980. [PubMed: 15034619] (b) Guimarães CRW, Repasky MP, Chandrasekhar J, Tirado-Rives J, Jorgensen WL. *J. Am. Chem. Soc.* 2003; 125:6892–6899. [PubMed: 12783541] (c) Štrajbl M, Shurki A, Kato M, Warshel A. *J. Am. Chem. Soc.* 2003; 125:10228–10237. [PubMed: 12926945] (d) Zhang X, Zhang X, Bruice TC. *Biochemistry.* 2005; 44:10443–10448. [PubMed: 16060652] (e) Khanjin NA, Snyder JP, Menger FM. *J. Am. Chem. Soc.* 1999; 121:11831–11846. (f) Guo H, Cui Q, Lipscomb WN, Karplus M. *Proc. Natl. Acad. Sci. U.S.A.* 2001; 98:9032–9037. [PubMed: 11481470] (g) Guo H, Cui Q, Lipscomb WN, Karplus M. *Angew. Chem. Int. Ed.* 2003; 42:1508–1511. (h) Martí S, Andrés J, Moliner V, Silla E, Tuñón I, Bertrán J, Field MJ. *J. Am. Chem. Soc.* 2001; 123:1709–1712. [PubMed: 11456771] (i) Garcia-Viloca M, Gao J, Karplus M, Truhlar DG. *Science.* 2004; 303:186–195. [PubMed: 14716003]
8. (a) Kast P, Asif-Ullah M, Jiang N, Hilvert D. *Proc. Natl. Acad. Sci. U.S.A.* 1996; 93:5043–5048. [PubMed: 8643526] (b) Cload ST, Liu DR, Pastor RM, Schultz PG. *J. Am. Chem. Soc.* 1996; 118:1787–1788. (c) Liu DR, Cload ST, Pastor RM, Schultz PG. *J. Am. Chem. Soc.* 1996; 118:1789–1790.
9. Kienhöfer A, Kast P, Hilvert D. *J. Am. Chem. Soc.* 2003; 125:3206–3207. [PubMed: 12630863]
10. Catalytic antibodies that accelerate the sigmatropic rearrangement of chorismate on the order of  $10^2$ - $10^4$ -fold: Jackson DY, Jacobs JW, Sugawara R, Reich SH, Bartlett PA, Schultz PG. *J. Am. Chem. Soc.* 1988; 110:4841–4842. (b) Jackson DY, Liang MN, Bartlett PA, Schultz PG. *Angew. Chem. Int. Ed.* 1992; 31:182–183. (c) Hilvert D, Carpenter SH, Nared KD, Auditor MT. *Proc. Natl. Acad. Sci. U.S.A.* 1988; 85:4953–4955. [PubMed: 3393525] (d) Hilvert D, Nared KD. *J. Am. Chem. Soc.* 1998; 110:5593–5594.

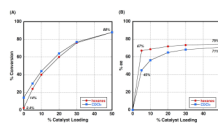
11. (a) Wiest O, Houk KN. *J. Org. Chem.* 1994; 59:7582–7584.(b) Wiest O, Houk KN. *J. Am. Chem. Soc.* 1995; 117:11628–11639.(c) Mader MM, Bartlett PA. *Chem. Rev.* 1997; 97:1281–1301. [PubMed: 11851452]
12. Haynes MR, Stura EA, Hilvert D, Wilson IA. *Science.* 1994:646–652. [PubMed: 8303271]
13. Uyeda C, Jacobsen EN. *J. Am. Chem. Soc.* 2008; 130:9228–9229. [PubMed: 18576616]
14. Solvent effects in the Claisen rearrangement: Coates RM, Rogers BD, Hobbs SJ, Curran DP, Peck DR. *J. Am. Chem. Soc.* 1987; 109:1160–1170. (b) Brandes E, Grieco PA, Gajewski JJ. *J. Org. Chem.* 1989; 54:515–516.(c) White WN, Wolfarth EF. *J. Org. Chem.* 1970; 35:2196–2199.
15. Rate acceleration by ureas and thioureas: Curran DP, Lung HK. *Tetrahedron Lett.* 1995; 36:6647–6650. Kirsten M, Rehbein J, Hiersemann M, Strassner T. *J. Org. Chem.* 2007; 72:4001–4011. [PubMed: 17477575]
16. (a) Dougherty DA. *Science.* 1996; 271:163–168. [PubMed: 8539615] (b) Zacharias N, Dougherty DA. *Trends Pharmacol. Sci.* 2002; 23:281–287. [PubMed: 12084634] (c) Thoma R, Schulz-Gasch T, D'Arcy B, Benz J, Aebi J, Dehmlow H, Hennig M, Stihle M, Ruf A. *Nature.* 2004; 432:118–122. [PubMed: 15525992] (d) Hoshino T, Sato T. *Chem. Commun.* 2002:291–301.(e) Wendt WK, Schultz GE, Corey EJ, Liu DR. *Angew. Chem. Int. Ed.* 2000; 39:2812–2833.
17. A more comprehensive account of catalyst optimization studies is included in the Supporting Information.
18. A review of non-linear effects in asymmetric synthesis: Kagan HB. *Adv. Synth. Catal.* 2001; 343:227–233.
19. Plots of product **6** ee and conversion as a function of catalyst (**R,R**)-**2** ee for rearrangements conducted in both hexanes and CDCl<sub>3</sub> are included in the Supporting Information.
20. A review of reaction progress kinetic analysis conducted under synthetically relevant conditions: Blackmond DG. *Angew. Chem. Int. Ed.* 2005; 44:4302–4320.
21. Examples of kinetic investigations of asymmetric reactions catalyzed by organic small molecules: Zuend SJ, Jacobsen EN. *J. Am. Chem. Soc.* 2007; 129:15872–15883. [PubMed: 18052247] (b) Zuend SJ, Jacobsen EN. *J. Am. Chem. Soc.* 2009; 131:15358–15374. [PubMed: 19778044] (c) Zotova N, Franzke A, Armstrong A, Blackmond DG. *J. Am. Chem. Soc.* 2007; 129:15100–15101. [PubMed: 18001021]
22. Detailed procedures for data acquisition and processing are included in the Supporting Information. <sup>1</sup>H-NMR signal integration was used to generate [5] data as a function of time. Rate vs. concentration plots were obtained from fits of the concentration vs. time data to high-order polynomial functions using the least-squares method, followed by differentiation of that function with respect to time. These data were parsed at 5% conversion intervals for the purposes of plotting and derivation of the rate law.
23. Rate constants and activation parameters for the rearrangements of various ester-substituted allyl vinyl ethers: Rehbein J, Leick S, Hiersemann M. *J. Org. Chem.* 2009; 74:1531–1540. [PubMed: 19152265]
24. Huang Y, Rawal VH. *J. Am. Chem. Soc.* 2002; 124:9662–9663. [PubMed: 12175197]
25. Frisch, MJ., et al. *Gaussian 03, Revision E.01*; Gaussian, Inc. Wallingford, CT: 2004.
26. (a) Meyer MP, DelMonte AJ, Singleton DA. *J. Am. Chem. Soc.* 1999; 121:10865–10874.(b) Aviyente V, Yoo HY, Houk KN. *J. Org. Chem.* 1997; 62:6121–6128.(c) Guner V, Khuong KS, Leach AG, Lee PS, Bartberger MD, Houk KN. *J. Phys. Chem. A.* 2003; 107:11445–11459.
27. For computational studies of the thermal, aqueous, and thiourea-catalyzed rearrangements of ester- and carboxylate-substituted allyl vinyl ethers, see refs 10b, 15b, and: Rehbein J, Hiersemann M. *J. Org. Chem.* 2009; 74:4336–4342. [PubMed: 19435361] Cramer CJ, Truhlar DG. *J. Am. Chem. Soc.* 1992; 114:8794–8799.
28. For consistency, *s-trans* is used here to describe an antiperiplanar relationship between the vinyl ether and ester carbonyl oxygen atoms about the intervening single bond, and *s-cis*, a synperiplanar geometry.
29. Zero-point vibrational energy corrections and free energies for all stationary points are included in the Supporting Information.
30. The energetic preference for  $\alpha$ -ketoesters to adopt a dipole-minimized, *s-trans* conformation, which precludes chelation of the two carbonyl oxygen atoms by a catalyst, provides a possible

rationale for the general observation of catalytic turnover in both Lewis and Brønsted acid-mediated Claisen rearrangements of *O*-allyl  $\alpha$ -ketoester substrates.

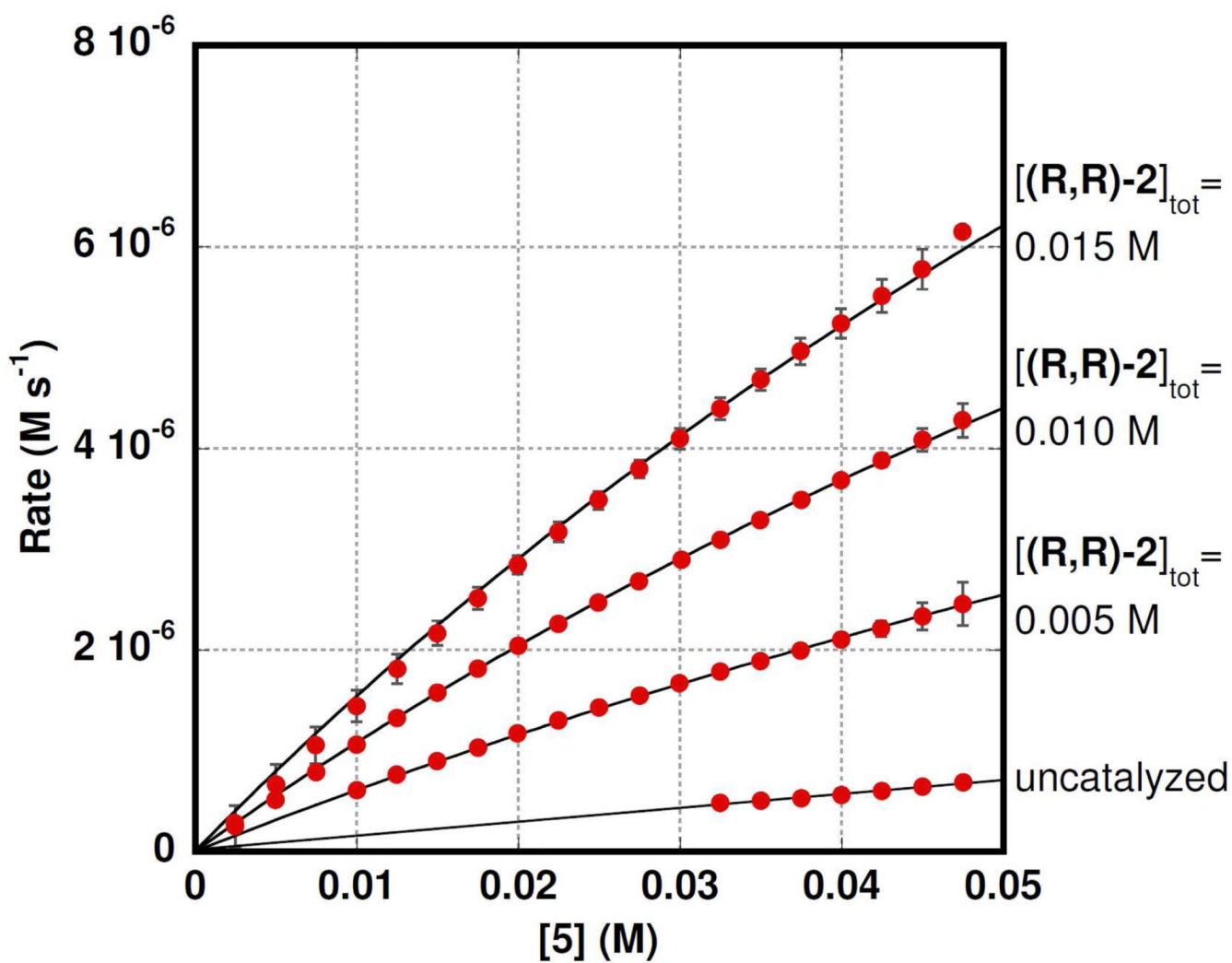
31. In ref 10b, an analogous shortening of an amidinium ion proton to ether oxygen distance was observed in the transition state for the Claisen rearrangement of a carboxylate-substituted substrate.
32. Glendening, ED.; Reed, AE.; Carpenter, JE.; Weinhold, F. NBO Version 3.1. Pittsburgh, PA: Gaussian Inc.; 1990.
33. Breneman CM, Wiberg KB. *J. Comput. Chem.* 1990; 11:361–373.
34. For the binding of ammonium cation to pyrrole, an interaction energy of 22.05 kcal/mol and a nearest distance of 2.1 Å from a proton of ammonium to a carbon atom of the pyrrole were calculated at the B3LYP/6-31G(d,p) level of theory: Zhu W-L, Tan X-J, Puah CM, Gu J-D, Jiang H-L, Chen K-X, Felder CE, Silman I, Sussman JL. *J. Phys. Chem. A* 2000; 104:9573–9580.
35. Examples of complexation-induced downfield shifts of guanidinium ion protons in the presence of anionic guests: Echavarren A, Galan A, Lehn J-M, de Mendoza J. *J. Am. Chem. Soc.* 1989; 111:4994–4995. Dixon RP, Geib SJ, Hamilton AD. *J. Am. Chem. Soc.* 1992; 114:365–366.
36. Examples of similar complexation-induced upfield shifts for aliphatic hydrogen atoms in proximity to arene  $\pi$ -faces in host-guest complexes: Kobayashi K, Asakawa Y, Kikuchi Y, Toi H, Aoyama Y. *J. Am. Chem. Soc.* 1993; 115:2648–2654. (b) Ferrand Y, Crump MP, Davis AP. *Science*. 2007; 218:619–622. [PubMed: 17962557] (c) Biros SM, Bergman RG, Raymond KN. *J. Am. Chem. Soc.* 2007; 129:12094–12095. [PubMed: 17880087]
37. For a recent reviews and references therein: Fielding L. *Tetrahedron*. 2000; 56:6151–6170. Hirose K. *J. Inc. Phenom. Macrocyclic Chem.* 2001; 39:193–209.
38. (a) Job P. *Ann. Chim.* 1928; 9:113–203. (b) MacCarthy P. *Anal. Chem.* 1978; 14:2165.
39. A plot of  $\Delta\delta \times$  mole fraction of **5** vs. mole fraction of **5** reached a maximum at 0.5 at a constant total concentration ( $[\mathbf{5}] + [(\mathbf{R,R})\text{-}\mathbf{2}]$ ) of 0.1 M. See Supporting Information for details.
40. An average distance of 2.91 Å was measured for intermolecular polar C-H to  $\pi$  interactions in a database study of organic crystal structures: Umezawa Y, Tsuboyama S, Takahashi H, Uzawa J, Nishio M. *Tetrahedron*. 1999; 55:10047–10056.
41.  $\Delta\Delta E$  between the ground state pro-(*S,S*) and pro-(*R,R*) conformations of the (**R,R**)-**3-5** complex was calculated to be 2.57 kcal/mol.
42. From crystallographic measurements, the van der Waals radius of a hydrogen atom is estimated to be 1.09–1.20 Å: Bondi A. *J. Phys. Chem.* 1964; 68:441–451. Rowland RS, Taylor R. *J. Phys. Chem.* 1996; 100:7384–7391.
43. Effect of arene substituents on the strength of cation- $\pi$  interactions: Mecozzi S, West AP Jr, Dougherty DA. *J. Am. Chem. Soc.* 1996; 118:2307–2308. Ma JC, Dougherty DA. *Chem. Rev.* 1997; 97:1303–1324. [PubMed: 11851453]
44. Examples of the use unnatural amino acids to resolve specific cation- $\pi$  interactions in protein-ligand complexes: Zhong W, Gallivan JP, Yinong Z, Li L, Lester HA, Dougherty DA. *Proc. Natl. Acad. Sci. U.S.A.* 1998; 95:12088–12093. [PubMed: 9770444] Xiu X, Puskar NL, Shanata JAP, Lester HA, Dougherty DA. *Nature*. 2009; 458:534–537. [PubMed: 19252481]
45. Studies of cation- $\pi$  interactions in asymmetric catalysis: Cannizzaro CE, Houk KN. *J. Am. Chem. Soc.* 2002; 124:7163–7169. [PubMed: 12059242] Wei Y, Held I, Zipse H. *Org. Biomol. Chem.* 2006; 4:4223–4230. [PubMed: 17312979] (b) Li X, Liu P, Houk KN, Birman VB. *J. Am. Chem. Soc.* 2008; 130:13836–13837. [PubMed: 18817392] (c) Knowles RR, Lin S, Jacobsen EN. *J. Am. Chem. Soc.* 2010; 132:5030–5032. [PubMed: 20369901]
46. Because of the large size of the systems being modeled and the presence of multiple small vibrational frequencies, zero-point vibrational energy corrections and free energies, derived from frequency calculations using the rigid-rotor/harmonic oscillator approximation, were not used to estimate enantioselectivities.
47. Selected examples of correlations between experimental and calculated enantioselectivities in catalytic reactions, see ref 21b and: Schneebeli ST, Hall ML, Breslow R, Friesner R. *J. Am. Chem. Soc.* 2009; 131:3965–3973. [PubMed: 19243187] (b) Kozłowski MC, Dixon SL, Panda M, Lauri G. *J. Am. Chem. Soc.* 2003; 125:6614–6615. [PubMed: 12769554] (c) Donoghue PJ, Helquist P, Norrby P-O, Wiest O. *J. Am. Chem. Soc.* 2009; 131:410–411. [PubMed: 19140780]

48. For comparisons of functionals for systems involving weak non-covalent interactions, see ref 21a, 21b, 45b and: Zhao Y, Truhlar DG. *J. Chem. Theory Comput.* 2007; 3:289–300. Zhao Y, Truhlar DG. *Acc. Chem. Res.* 2008; 41:157–167. [PubMed: 18186612]
49. Examples of C-F...M interactions between fluoroarenes and metal cation interactions in crystal structures: Plenio H. *Chem. Rev.* 1997; 97:3363–3384. [PubMed: 11851493] (b) Kulawiec RJ, Crabtree RH. *Coord. Chem. Rev.* 1990; 99:89–115.(c) Bouwkamp MW, Budzelaar PHM, Gercama J, Morales IDHM, de Wolf J, Meetsma A, Troyanov SI, Teuben JH, Hessen B. *J. Am. Chem. Soc.* 2005; 127:14310–14319. [PubMed: 16218625]
50. Examples of C-F...H-C contacts of 2.2–2.8 Å in fluoroarene-arene crystal structures: Shimoni L, Glusker JP. *Structural Chemistry.* 1994; 5:383–397. (b) Ngola SM, Dougherty DA. *J. Org. Chem.* 1998; 63:4566–4567.(c) Smith CE, Smith PS, Thomas RL, Robins EG, Collings JC, Dai C, Scott AJ, Borwick S, Batsanov AS, Watt SW, Clark SJ, Viney C, Howard JAK, Clegg W, Marder TB. *J. Mater. Chem.* 2004; 14:413–420.
51. (a) Pawlak J, Padykula RE, Kronis JD, Aleksejczyk RA, Berchtold GA. *J. Am. Chem. Soc.* 1989; 111:3374–3381.(b) Galopin CC, Ganem B. *Bioorg. Med. Chem. Lett.* 1997; 7:2885–2886.
52. For a broader discussion of computational approaches to the elucidation of asymmetric catalytic mechanisms, see: Houk KN, Cheong PH-Y. *Nature.* 2008; 455:309–313. [PubMed: 18800129]
53. (a) Taylor MS, Jacobsen EN. *Angew. Chem. Int. Ed.* 2006; 45:1520–1543.(b) Knowles RR, Jacobsen EN. *Proc. Natl. Acad. Sci. USA.* 2010; 107:20678–20685. [PubMed: 20956302]

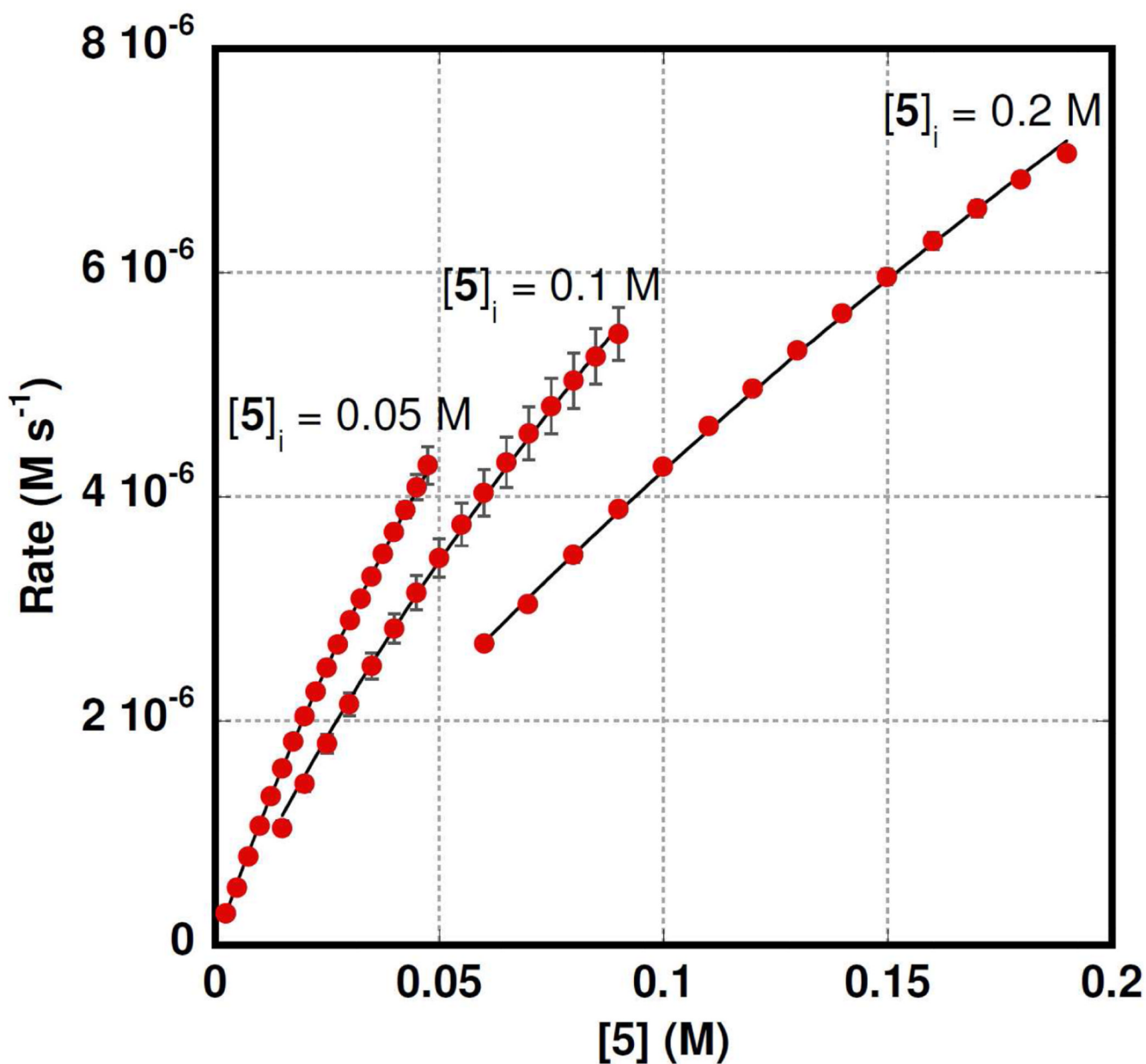




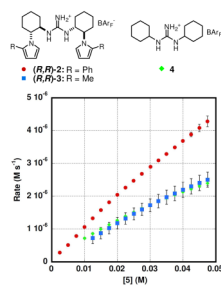
**Figure 1.** Dependence of (A) conversion and (B) product **6** ee on catalyst (**R,R**)-**2** loading in hexanes and CDCl<sub>3</sub>. Reactions were conducted at 40 °C for 14 h.



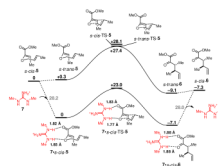
**Figure 2.** Rate profiles for reactions with various loadings of catalyst  $(R,R)$ -2 ( $[(R,R)$ -2] $_{tot} = 0.005$ – $0.02 M$ ;  $[5]_i = 0.05 M$ ;  $55 ^\circ C$ ,  $CDCl_3$ ). Each set of points is the average rate determined from two individual kinetics experiments with the error bars representing the range of measurements. The curves are best fits of the rate vs. concentration data to eq 1.



**Figure 3.** Rate profiles for reactions with various initial concentrations of **5** ( $[(R,R)\text{-2}]_{\text{tot}} = 0.01 \text{ M}$ ;  $[\mathbf{5}]_i = 0.05\text{--}0.2 \text{ M}$ ;  $55 \text{ }^\circ\text{C}$ ,  $\text{CDCl}_3$ ). Each set of points is the average rate determined from two individual kinetics experiments with the error bars representing the range of measurements. The curves are best fits of the rate vs. concentration data to eq 1.

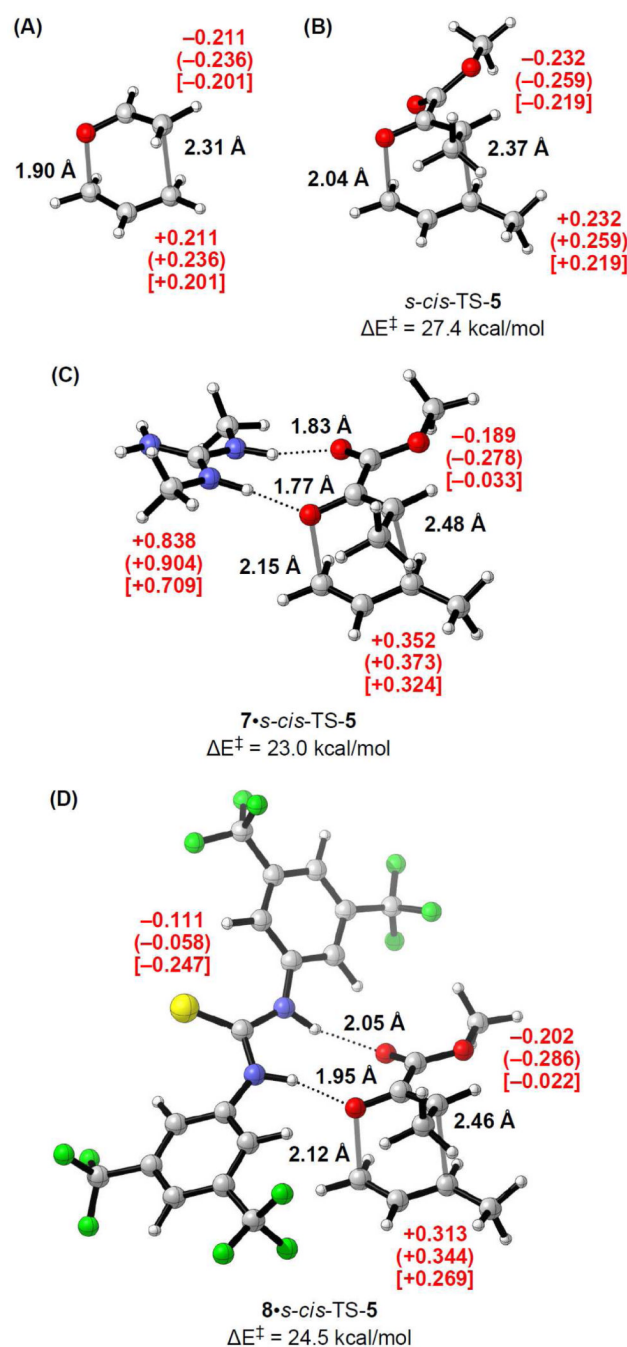


**Figure 4.** Rate profiles for the rearrangement of **5**, catalyzed by **(R,R)-2** (red circles), **(R,R)-3** (blue squares), and **4** (green diamonds). [cat]<sub>tot</sub> = 0.01 M; [**5**]<sub>i</sub> = 0.05 M; 55 °C, CDCl<sub>3</sub>.

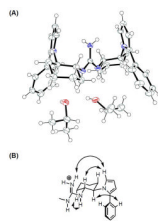


**Figure 5.** Energy diagram for the uncatalyzed (top pathway) and *N,N'*-dimethylguanidinium- (7) catalyzed (bottom pathway) rearrangement of **5** to **6**. All stationary points are fully optimized at the B3LYP/6-31G(d) level of theory and verified by frequency analysis. Uncorrected electronic energies in kcal/mol are relative to the lowest-energy structure of the substrate or catalyst–substrate complex. Distances for hydrogen-bonding interactions are shown in Angstroms.

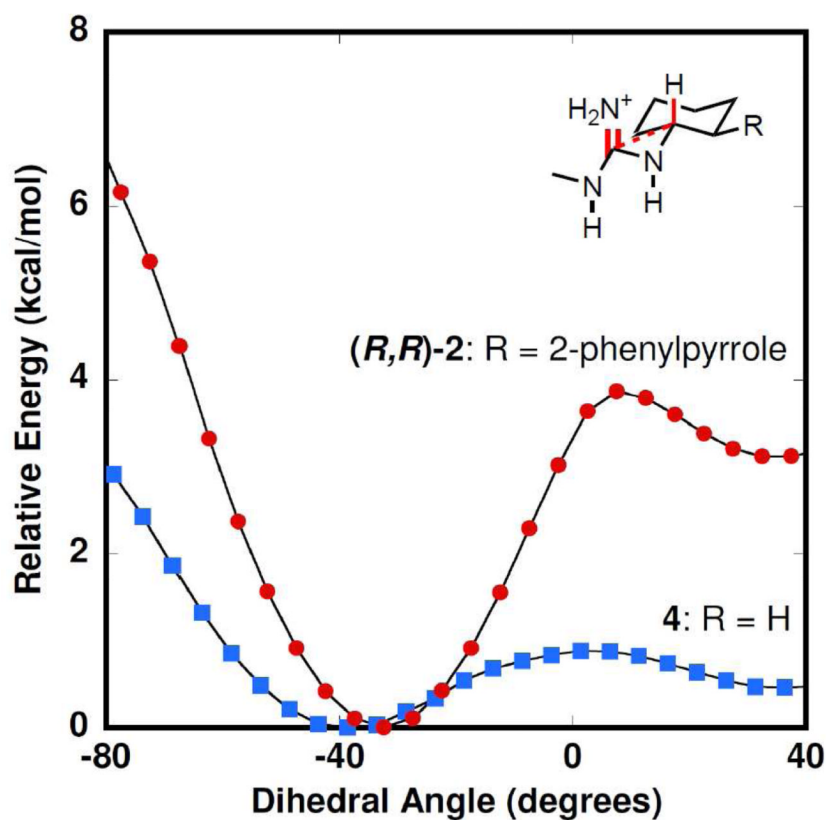
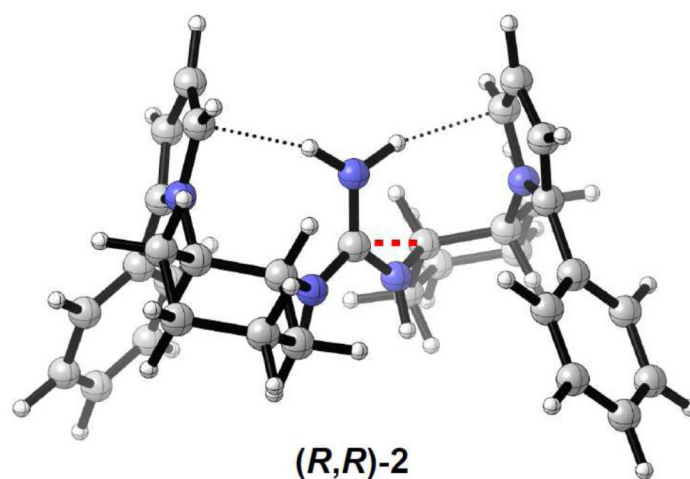


**Figure 6.**

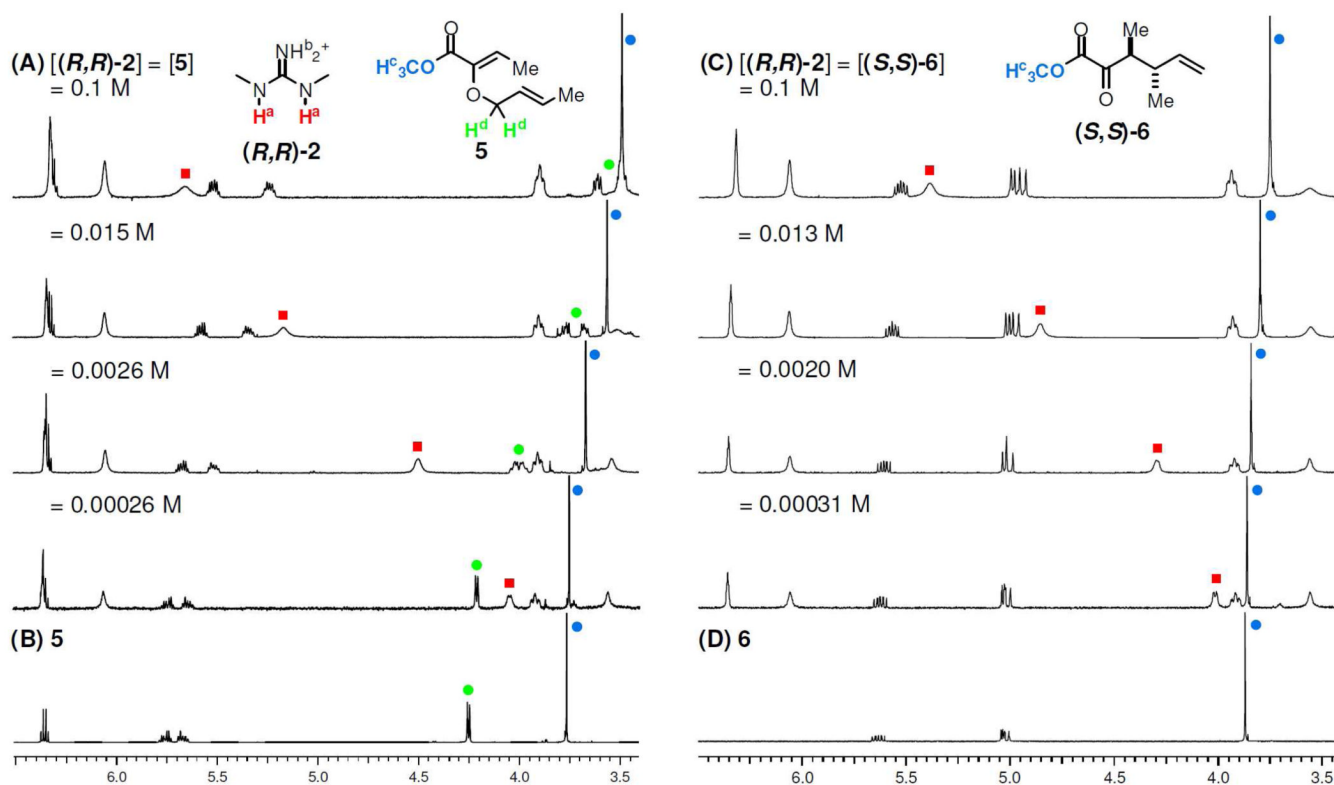
Calculated transition structures at the B3LYP/6-31G(d) level of theory for (A) the uncatalyzed rearrangement of allyl vinyl ether, (B) the uncatalyzed rearrangement of **5**, (C) the rearrangement of **5** catalyzed by guanidinium ion **7**, and (D) the rearrangement of **5** catalyzed by thiourea **8**. Distances for the breaking C–O and forming C–C bonds as well as hydrogen-bonds are in Angstroms. Mulliken charges, NBO charges in parentheses, and CHELPG charges in square brackets for the oxallyl and allyl fragments as well as the guanidinium ion are shown in red.



**Figure 7.** (A) 50% probability ellipsoid representation of the X-ray structure of (***R,R***)-**2** co-crystallized with two isopropanol molecules. The counterion is omitted for clarity. (B) Selected ROESY cross-peaks for (***R,R***)-**2** in CDCl<sub>3</sub>.



**Figure 8.** (*Z,Z*)-geometry of (*R,R*)-**2** optimized at the B3LYP/6-31G(d) level of theory and scan of the dihedral angle between the C–NH<sub>2</sub> bond of the guanidinium ion and the axial C–H bond of the cyclohexane ring highlighted in red.

**Figure 9.**

(A)  $^1\text{H-NMR}$  dilutions of a 1:1 mixture of  $(R,R)$ -**2** and **5** in  $\text{CDCl}_3$  (0.1–0.00026 M) and (B) the free substrate **5**. (C)  $^1\text{H-NMR}$  dilutions of a 1:1 mixture of  $(R,R)$ -**2** and 80% ee  $(S,S)$ -**6** in  $\text{CDCl}_3$  (0.1–0.00031 M) and (D) the free product **6**.

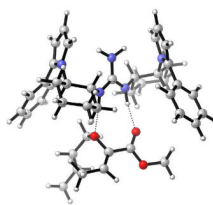


**Figure 10.**  
**(R,R)-2•pro-(S,S)-5** complex optimized at the B3LYP/6-31G(d) level of theory.



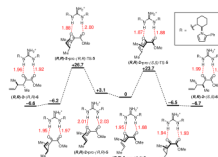


**Figure 11.**

Energy diagram for the asymmetric rearrangement of **5** to **6**, catalyzed by **(R,R)-2**. All stationary points are fully optimized at the B3LYP/6-31G(d) level of theory and verified by frequency analysis. Uncorrected electronic energies in kcal/mol are relative to **(R,R)-2**•pro-(*S,S*)-**5**. Distances for hydrogen-bonding interactions are shown in Angstroms.

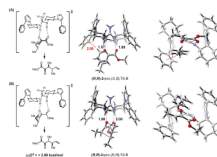


**Figure 12.** Fully optimized diastereomeric transition structures for the rearrangement of **5** catalyzed by **(R,R)-2** leading to the (A) major pro-(*S,S*) and (B) minor pro-(*R,R*) enantiomers of product (B3LYP/6-31G(d)). Key distances for non-covalent interactions are shown in Angstroms.

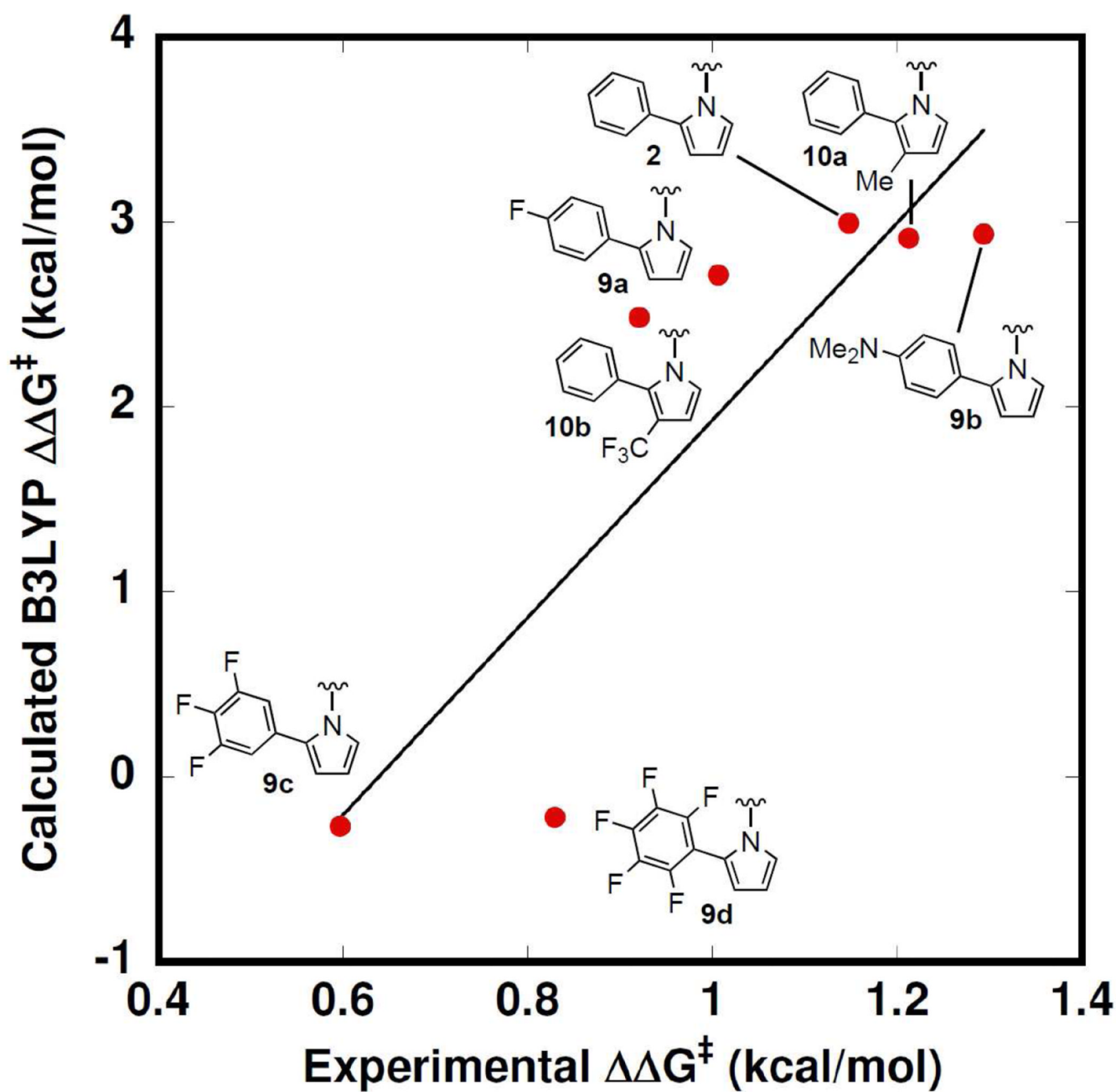


**Figure 13.** Experimental vs. calculated B3LYP enantioselectivity. The black line represents a least-squares fit to a linear function (intercept:  $-3.41$ , slope:  $5.33$ ,  $R^2 = 0.74$ ).

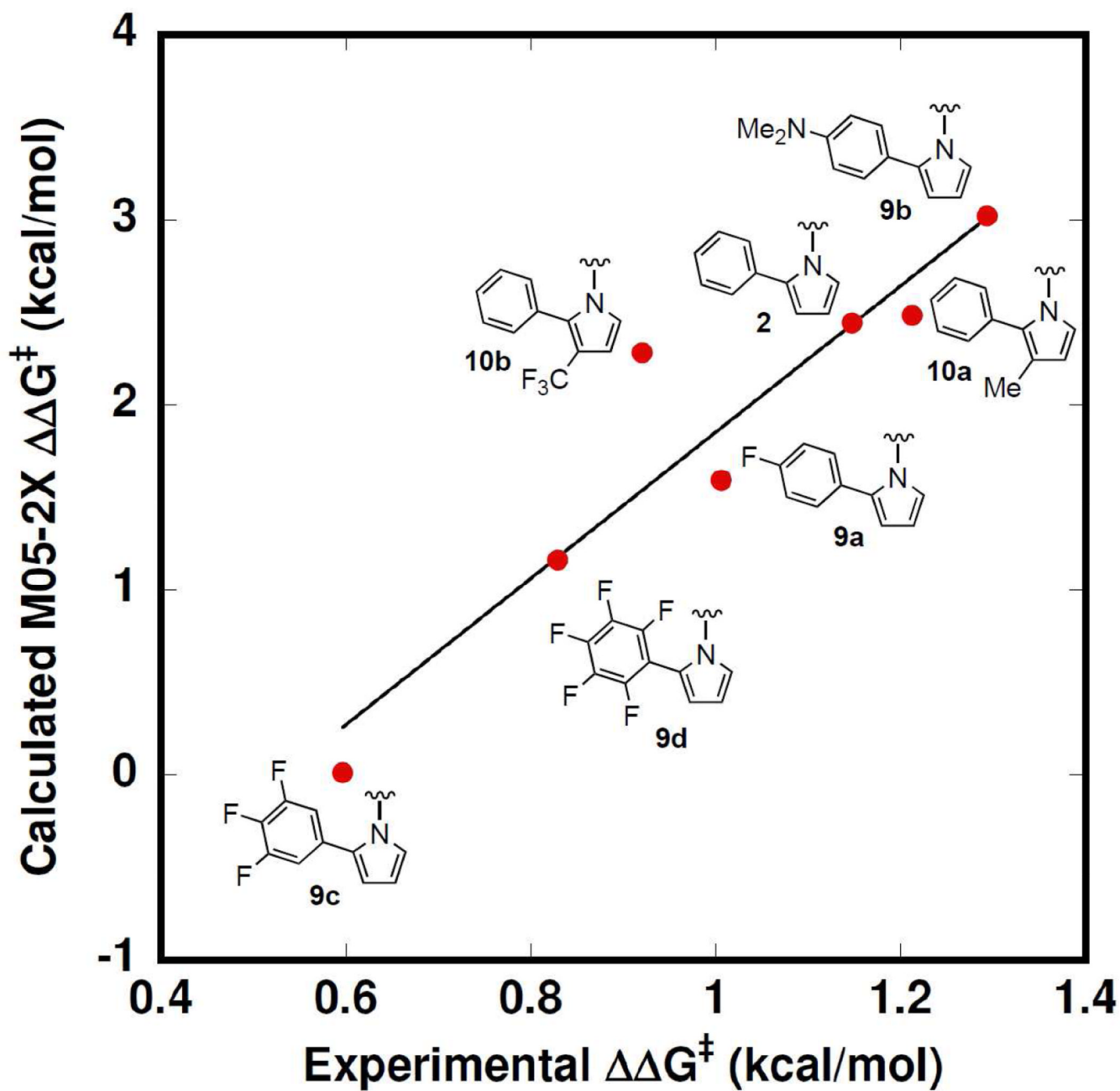


**Figure 14.** Experimental vs. calculated M05-2X enantioselectivity. The black line represents a least-squares fit to a linear function (intercept:  $-2.10$ , slope:  $3.95$ ,  $R^2 = 0.88$ ).

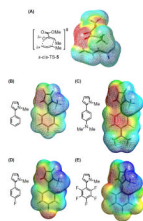


**Figure 15.**

Electrostatic potential maps for fully optimized structures (B3LYP/6-31G(d)) of (A) the rearrangement transition state for **5** and *N*-methyl (B) 2-phenylpyrrole, (C) 2-(4-(dimethylamino)phenyl)pyrrole, (D) 2-(4-fluorophenyl)pyrrole, and (E) 2-pentafluorophenylpyrrole. Negative potentials are shown in red and positive potentials in blue.

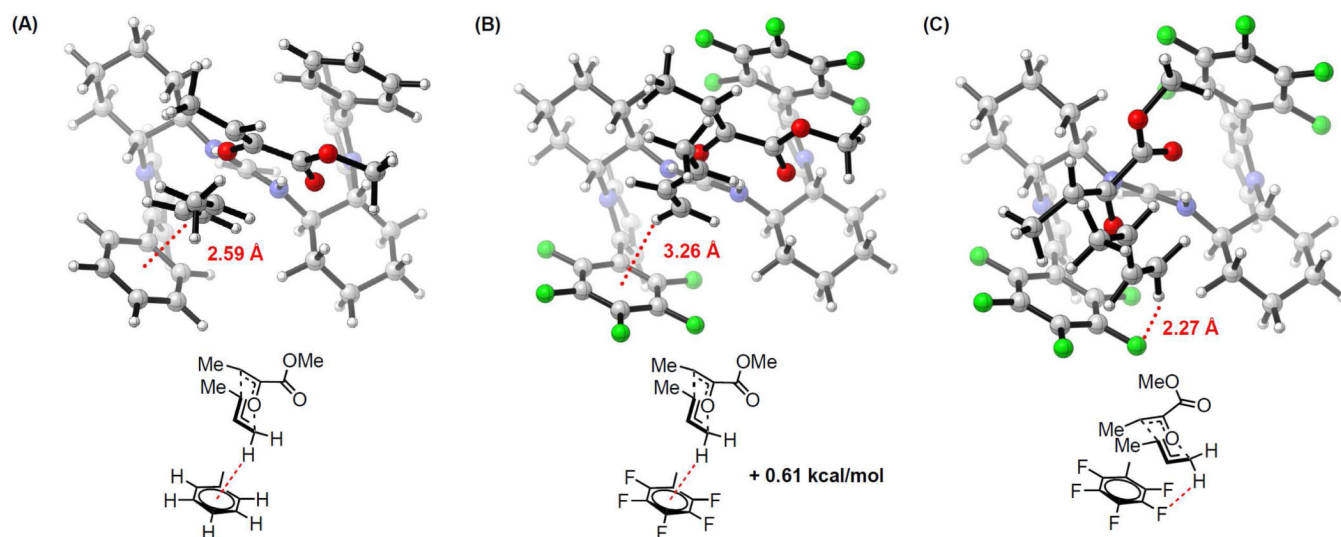
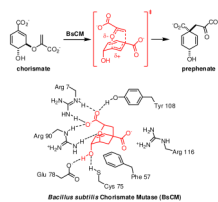
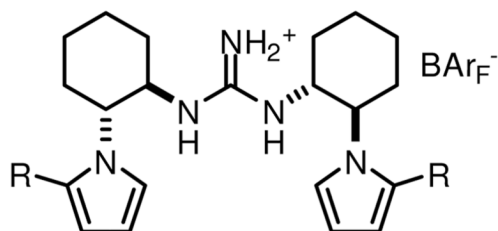
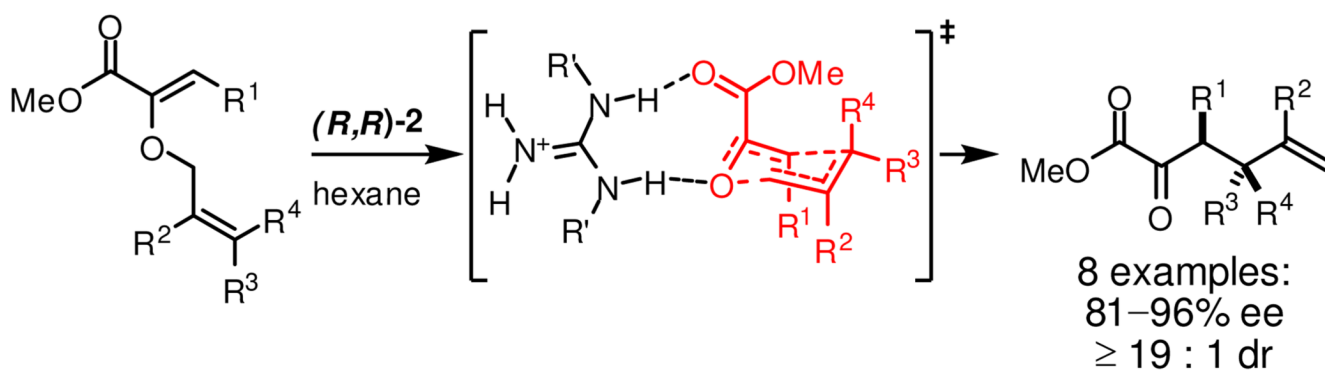


**Figure 16.** pro-(*S,S*) transition structures for (A) catalyst **2** and for the pentafluoro-substituted catalyst **9d** highlighting interactions of the cationic allyl fragment with (B) the  $\pi$ -face of the arene and (C) the meta-fluorine substituent (M05-2X/6-31G(d)). The relative energy of structures (B) and (C) is shown.

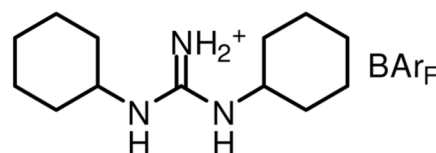


**Scheme 1.**  
Hydrogen-Bonding Interactions in the Structure of *Bacillus subtilis* Chorismate Mutase Bound to the Oxabicyclic Transition State Analog **1**.



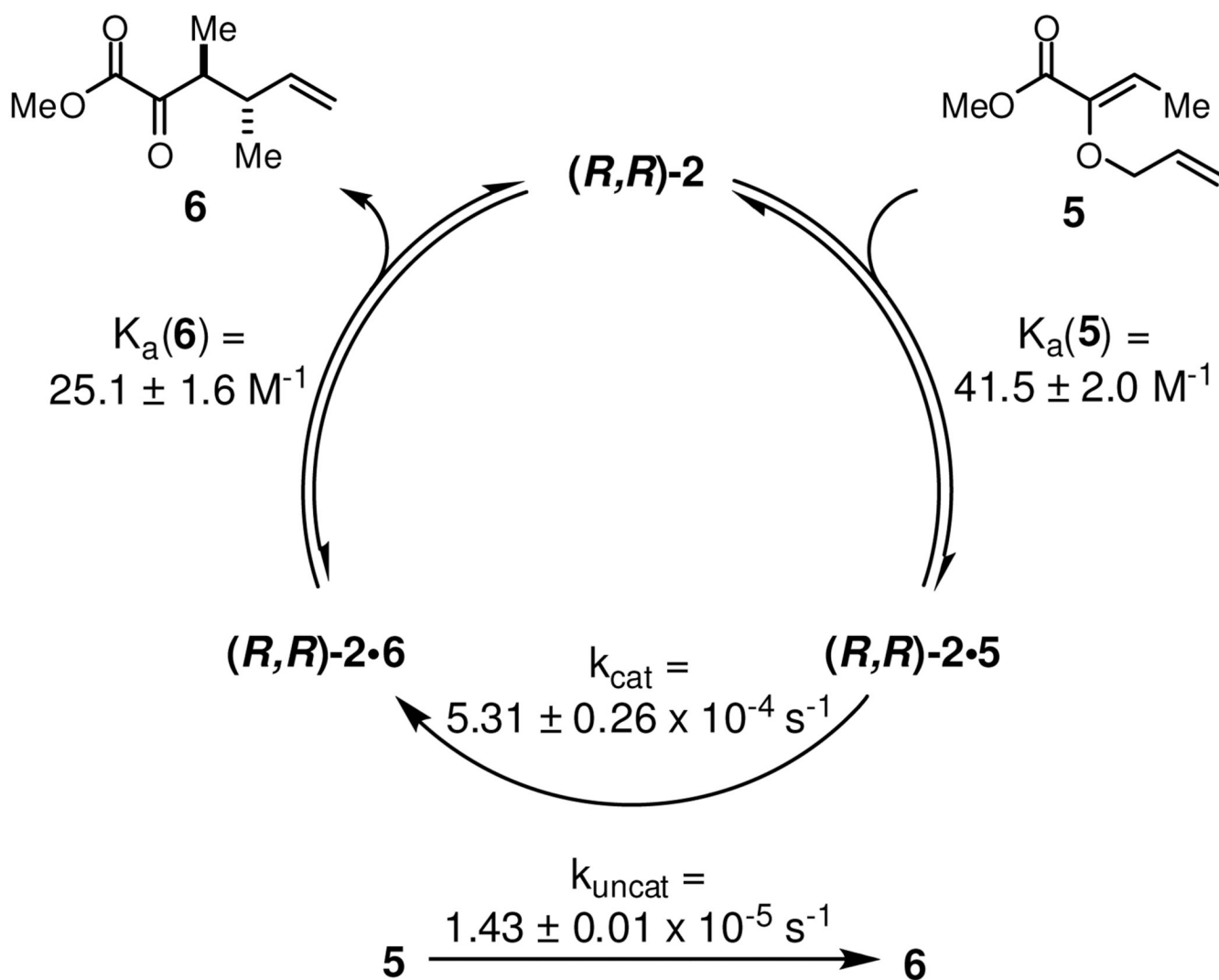


**(*R,R*)-2:** R = Ph  
**(*R,R*)-3:** R = Me



**4**

**Scheme 2.**  
Enantioselective Claisen Rearrangement of *O*-allyl  $\alpha$ -ketoesters Catalyzed by Pyrrole-Substituted Guanidinium Catalysts.



**Scheme 3.**  
Rate and Equilibrium Constants for Catalyzed and Uncatalyzed Rearrangements of **5** in  $\text{CDCl}_3$ .

**Table 1**

Dependence of Conversion and Product ee on Catalyst Structure and Solvent



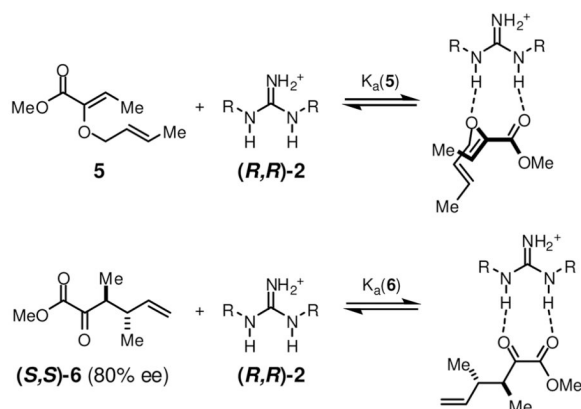
entry	catalyst	solvent	conversion <sup>a</sup>	ee <sup>b</sup>
1	( <i>R,R</i> )-2	hexanes	85%	73%
2	( <i>R,R</i> )-3	hexanes	59%	41%
3	( <i>R,R</i> )-2	toluene	82%	72%
4	( <i>R,R</i> )-2	CH <sub>2</sub> Cl <sub>2</sub>	83%	65%
5	( <i>R,R</i> )-2	CDCl <sub>3</sub>	79%	66%
6	( <i>R,R</i> )-2	TBME	16%	19%

<sup>a</sup> Conversions were determined from crude reaction mixtures by <sup>1</sup>H-NMR signal integration. All rearrangements afforded product **6** with a > 20:1 d.r.

<sup>b</sup> Enantiomeric excesses of purified products were determined by GC analysis using commercial chiral columns.

Table 2

## Binding Constant Measurements



entry	catalyst	substrate/product	$K_a \text{ M}^{-1}$ <sup>a</sup>
1	<b>(R,R)-2</b>	<b>5</b>	$218 \pm 14$
2	<b>(R,R)-2</b>	<b>(S,S)-6</b> (80% ee)	$108 \pm 4$
3	<b>(S,S)-2</b>	<b>(S,S)-6</b> (80% ee)	$107 \pm 4$

<sup>a</sup> Association constants for a 1:1 complex between the guanidinium ion **2** and **5** or **6**. Uncertainties are standard errors of the curve fit.

**Table 3**

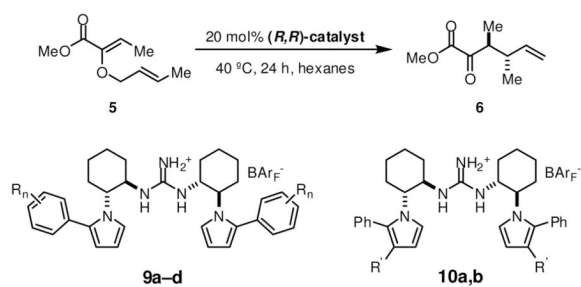
## Comparison of Computational Methods

computational method	$\Delta\Delta E^\ddagger$ (kcal/mol) <sup>a</sup>
B3LYP/6-31G(d)	2.99 (2.89)
B3LYP/6-311+G(d,p)//B3LYP/6-31G(d)	3.24
MP2/6-31G(d)//B3LYP/6-31G(d)	2.69
M05-2X/6-31G(d)	2.44 (2.47)
M05-2X/6-31+G(d,p)//M05-2X/6-31G(d)	2.55

<sup>a</sup>Uncorrected differences in transition state energies. Values in parentheses include an unscaled correction for zero-point vibrational energy.

Table 4

Dependence of Enantioselectivity on Catalyst Electronics




catalyst	catalyst substituents	expt. e.r. <sup>a</sup>	expt. $\Delta\Delta G^\ddagger$ (kcal/mol) <sup>b</sup>
<b>2</b>	-	6.33 ± .05	1.15 ± 0.01
<b>9a</b>	R = 4-fluoro	5.05 ± .12	1.01 ± .01
<b>9b</b>	R = 4-dimethylamino	8.01 ± 0.20	1.29 ± 0.02
<b>9c</b>	R = 3,4,5-trifluoro	2.61 ± 0.01	0.597 ± 0.002
<b>9d</b>	R = 2,3,4,5,6-pentafluoro	3.80 ± 0.01	0.830 ± 0.001
<b>10a</b>	R' = methyl	7.03 ± 0.03	1.21 ± 0.01
<b>10b</b>	R' = trifluoromethyl	4.40 ± 0.05	0.92 ± 0.01

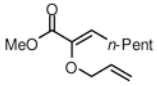
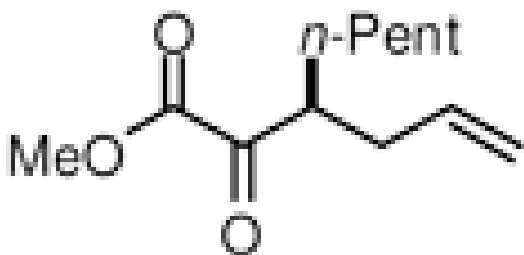
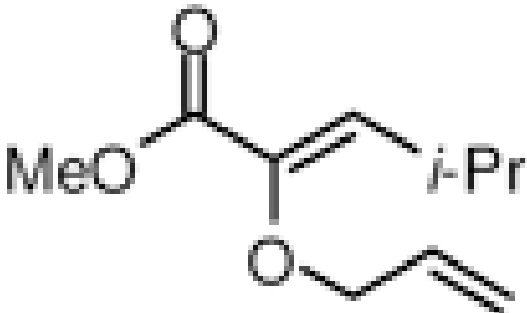
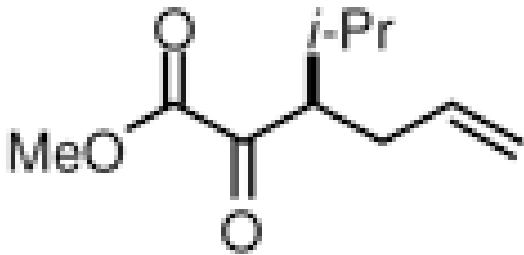
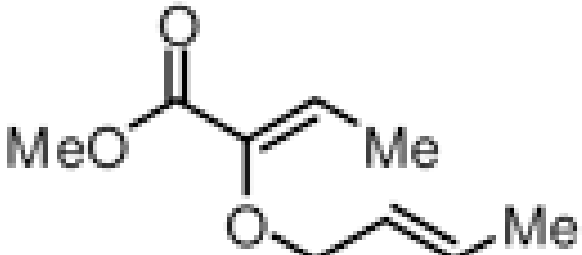
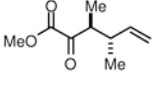
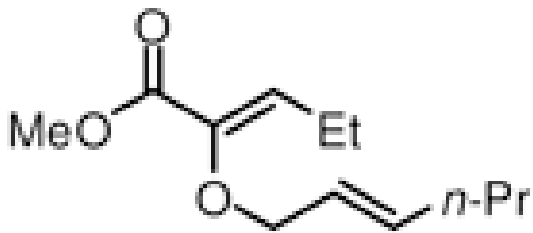
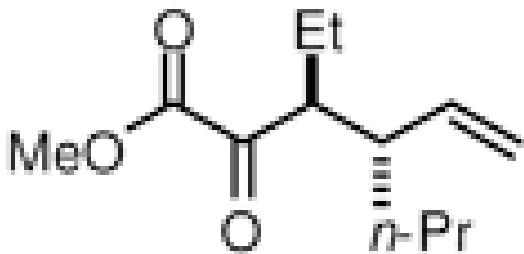
<sup>a</sup>Enantiomeric ratios are averages of two experiments with the error bars representing the range of results.

<sup>b</sup>Relative activation free energies were estimated according to classical transition state theory ( $\Delta\Delta G^\ddagger = -RT \ln \left( \frac{[(S,S)\text{-}6]}{[(R,R)\text{-}6]} \right)$ , T = 313.15 K).

Table 6

Substrate Scope and Comparison of Catalysts **2** and **9b**.<sup>a</sup>



entry	substrate	product	time/temp	cat yield
1			30 °C / 6 d	82%
2			30 °C / 12 d	81%
3			30 °C / 72 h	92%
4			30 °C / 8 d	88%





entry	substrate	product	time/temp	cat yield
5			40 °C / 12 d	76%
6			40 °C / 8 d	90%
7			40 °C / 12 d	75%

<sup>a</sup>Reactions run on a 0.1 mmol scale in 2 mL of hexanes using a 20 mol% loading of catalyst (*R,R*-**2** or (*R,R*)-**9b**).

<sup>b</sup>Isolated yields following purification by silica gel chromatography.

<sup>c</sup>Diastereomeric ratios determined from <sup>1</sup>H-NMR spectra of the crude reaction mixture.

<sup>d</sup>Enantiomeric excesses determined by GC or HPLC analysis using commercial chiral columns (see Supporting Information).